Geometric Mismatches within the Concentric Layers of Rotavirus Particles: a Potential Regulatory Switch of Viral Particle Transcription Activity

Article *in* Journal of Virology · April 2008

DOI: 10.1128/JVI.02268-07 · Source: PubMed

CITATIONS
20

READS
208

9 authors, including:

Xavier Siebert
Université de Mons
46 PUBLICATIONS **295** CITATIONS
SEE PROFILE

Malika Ouldali
French National Centre for Scientific Research
12 PUBLICATIONS **194** CITATIONS
SEE PROFILE

Leandro F. Estrozi
French National Centre for Scientific Research
53 PUBLICATIONS **625** CITATIONS
SEE PROFILE

Jorge Navaza
Ecole normale supérieure de Cachan
123 PUBLICATIONS **13,509** CITATIONS
SEE PROFILE

JOURNAL OF VIROLOGY, Mar. 2008, p. 2844–2852 Vol. 82, No. 6
0022-538X/08/$08.00+0 doi:10.1128/JVI.02268-07

Geometric Mismatches within the Concentric Layers of Rotavirus Particles: a Potential Regulatory Switch of Viral Particle Transcription Activity▽

Sonia Libersou,† Xavier Siebert,†‡ Malika Ouldali, Leandro F. Estrozi,‡ Jorge Navaza,‡ Annie Charpilienne, Pascale Garnier, Didier Poncet, and Jean Lepault*

Laboratoire de Virologie Moléculaire et Structurale, CNRS, UMR 2472, IFR 115, INRA, UMR 1157, 1 Avenue de la Terrasse, F-91198 Gif-sur-Yvette, France

Received 19 October 2007/Accepted 26 December 2007

Rotaviruses are prototypical double-stranded RNA viruses whose triple-layered icosahedral capsid constitutes transcriptional machinery activated by the release of the external layer. To understand the molecular basis of this activation, we studied the structural interplay between the three capsid layers by electron cryo-microscopy and digital image processing. Two viral particles and four virus-like particles containing various combinations of inner (VP2)-, middle (VP6)-, and outer (VP7)-layer proteins were studied. We observed that the absence of the VP2 layer increases the particle diameter and changes the type of quasi-equivalent icosahedral symmetry, as described by the shift in triangulation number (T) of the VP6 layer (from T = 13 to T = 19 or more). By fitting X-ray models of VP6 into each reconstruction, we determined the quasi-atomic structures of the middle layers. These models showed that the VP6 lattices, i.e., curvature and trimer contacts, are characteristic of the particle composition. The different functional states of VP6 thus appear as being characterized by trimers having similar conformations but establishing different intertrimeric contacts. Remarkably, the external protein VP7 reorients the VP6 trimers located around the fivefold axes of the icosahedral capsid, thereby shrinking the channel through which mRNA exits the transcribing rotavirus particle. We conclude that the constraints arising from the different geometries imposed by the external and internal layers of the rotavirus capsid constitute a potential switch regulating the transcription activity of the viral particles.

Rotaviruses are pathogens that still cause lethal gastroenteritis in both children and young animals. They are members of the *Reoviridae* family and are characterized by a nonenveloped multilayered protein capsid containing 11 segments of double-stranded RNA (dsRNA) that constitute the viral genome (13). X-ray crystallography studies revealed the complex structure of the icosahedral capsid of different *Reoviridae* viruses: blue tongue virus (19), reovirus (42), and rice dwarf virus (33). All *Reoviridae* viruses appear to possess a similar capsid organization made of several layers of proteins. These layers obey different icosahedral symmetries characterized by different triangulation numbers (T) (4). The consequences of these complex but conserved symmetry mismatches and in particular their implication in the virus morphogenesis and transcriptional activity are poorly understood.

The mature infectious rotavirus capsid is referred to as the triple-layered particle (TLP) because its capsid is composed of three protein layers: outer (proteins VP7 and VP4), middle (protein VP6), and inner (protein VP2). VP7 makes a T = 13*l* (*l* for levo) icosahedral lattice (29, 43) which defines three types of aqueous channels according to their position with respect to the icosahedral symmetry axes (41). VP4 is anchored in the channels surrounding the particle fivefold axes and protrudes by more than 10 nm from the particle surface (39, 49). The complete outer layer thus displays a T = 1 icosahedral lattice. To gain infectivity, virions must be activated by proteolysis (14). Trypsin, which has been found bound to TLP (3), cleaves VP4 to generate VP5*, a permeabilizing membrane protein (10, 34, 44), and VP8*, the rotavirus hemagglutinin (16). The structures of VP5* and of a large fragment of VP8* have been determined to atomic resolution (11, 12, 51). While VP4 plays a major role in the virus entry process, it may modulate intracellular signaling (23). VP6 also forms a T = 13*l* protein layer whose trimers interact with trimers of VP7 (41, 43, 50). Finally, 120 molecules of VP2 form the innermost layer of the TLP, obeying a T = 1 icosahedral lattice with two molecules in the icosahedral asymmetric unit. Additionally, the replication-transcription enzymes VP1 and VP3 are located near the icosahedral fivefold axes below VP2 (40). VP1 is an RNA-dependent RNA polymerase, and VP3 is a guanylylmethyltransferase. The capsid contains 11 segments of dsRNA that code for all the above-mentioned structural proteins (VP1 to -4, VP6, and VP7) and, depending upon the strain, five (NSP1 to -5) or six (NSP1 to -6) nonstructural proteins.

The outer layer of the TLP is lost when the virion enters into a target cell, giving rise to the so-called double-layered particle (DLP). In addition to playing a role in the virus entry process, the external layer of the TLP inhibits the transcription activity of the viral particle. Indeed, removal of VP4 and VP7 from TLP by calcium chelation activates the transcriptional activity of the viral particle (6). The structural basis for transcription inhibition is not clear, and several hypotheses have been proposed. First, proteins bound to VP6, such as VP7 or antibodies, appear to obstruct the type I channels located at the particle

* Corresponding author. Mailing address: Laboratoire de Virologie Moléculaire et Structurale, CNRS, UMR 2472, IFR 115, INRA, UMR 1157, 1 Avenue de la Terrasse, F-91198 Gif-sur-Yvette, France. Phone: (33) 1 69 82 38 55. Fax: (33) 1 69 82 43 08. E-mail: lepault@vms.cnrs-gif.fr.
† These authors contributed equally to this work.
‡ Present address: Institut de Biologie Structurale, 41, rue Jules Horowitz, F-38027 Grenoble Cedex 1, France.
▽ Published ahead of print on 9 January 2008.

fivefold axes (25); VP7 thus causes a steric hindrance that blocks the exit of the nascent mRNAs. Second, proteins that inhibit the transcription also appear to induce a structural change to VP6 (15, 24). Finally, VP6-bound proteins have been proposed to sterically hinder transient VP6 conformational changes essential to the transcription process (46).

To study the effect of VP7 and VP2 on the conformation and assembly of VP6, we studied several macromolecular complexes formed by VP6 with or without VP7 and with or without VP2. In all cases, spherical particles, generally called virus-like particles (VLPs), were formed. However, depending upon the VLP composition, the particles have different radii that reflect changes in VP6 intertrimer contacts and icosahedral lattices. Proteins constituting the different layers of the rotavirus capsid have thus the remarkable ability to form lattices with a wide variety of geometries and quasi-equivalent symmetries. The atomic structure of VP6 has been solved by X-ray crystallography and fitted into an electron microscopy (EM) three-dimensional (3-D) reconstruction of DLP (31) to produce a pseudo-atomic model of the VP6 layer. Within the viral particle, VP6 trimers associate through different contacts, some of which are very similar to those formed when VP6 assembles into helical assemblies (27). Here we extended this approach and determined the quasi-atomic models of the VP6 lattices in TLP, VLP2/6, VLP2/6/7, VLP6, and VLP6/7. This study suggests that the geometric mismatch between the different rotavirus capsid protein layers induces constraints that change the properties of the type I channel and thus regulate the transcription activity of rotavirus particles.

MATERIALS AND METHODS

VLP production and purification. VLPs were expressed and purified as previously described (22, 47). To produce each of the four VLPs, Sf9 cells were coinfected (5 PFU per cell) with different combinations of baculovirus recombinants BacRf2 (22), BacRf6 (47), and BacRf9 (17, 45), which code for the rotavirus proteins VP2, VP6, and VP7, respectively. The infected cells were collected at 5 or 7 days postinfection and extracted with Vertrel XF in a 20 mM PIPES [piperazine-*N*,*N*′-bis(2-ethanesulfonic acid)] buffer with 10 mM $CaCl_2$ (pH 6.6). CsCl was added to the aqueous phase containing VLPs to obtain a refractive index of 1.3620, and the mixture was centrifuged for 18 h at 35,000 rpm in a Beckman SW55 rotor. The bands containing the VLPs were then subjected to a second CsCl gradient centrifugation. The gradient fractions containing the VLPs were kept at −4°C, and salt was removed just before use with a spin column (Sephadex G25; Pharmacia) generally equilibrated in a buffer containing 5 mM Tris (pH 7.5) and 15 mM NaCl.

In order to reduce the polydispersity of VLP6/7, these particles were disassembled by chelating calcium by dialysis in a TNE buffer (50 mM Tris, 150 mM NaCl, 1 mM EDTA, pH 8) for 1 h at 4°C. They were then slowly reassembled at 4°C by addition of 10 mM $CaCl_2$.

Rotavirus VP6 was produced in Sf9 cells as above described and purified as described previously (37). Briefly, infected Sf9 cells were harvested at 3 to 5 days postinfection, and clarified medium was centrifuged for 30 min at 35,000 rpm in a Beckman 45 Ti rotor. The pellet was resuspended in 300 mM $CaCl_2$ and 50 mM MOPS (morpholinepropanesulfonic acid; pH 6) and centrifuged for 10 min at 13,000 × *g*. The supernatant was subjected to size exclusion chromatography (Superdex HR 10/30) using the same buffer. VLP6 was recovered after dialysis of the fractions corresponding to the major peak (VP6 trimers) in 50 mM sodium acetate–acetic acid, pH 4.5 (27).

TLP and DLP production and purification. The RF strain of rotavirus was multiplied in African green monkey kidney cells (MA104 cells). The cells, grown as monolayers in Eagle's minimum essential medium, were infected at a low multiplicity of infection (0.1 PFU per cell) in the presence of trypsin (0.44 μg/ml). Virus particles were extracted from infected cells with Vertrel XF as described previously (32). CsCl was then added to obtain a refractive index equal to 1.3690, and the mixture was centrifuged for 18 h at 35,000 rpm in a Beckman SW55 rotor. Upper (TLP) and lower (DLP) bands were collected and separately repurified on a CsCl gradient. Particles were kept suspended in CsCl at −4°C, a conservation method that maintains the infectivity of TLPs over weeks. Salt was removed with a spin column just before use (Sephadex G25; Pharmacia).

EM and image analysis. All samples were first controlled by conventional EM using uranyl acetate as a negative stain. Adequate samples were further studied by cryo-EM as described earlier (1). A drop of the suspension was deposited on a holey carbon film coated grid. The excess was blotted with a filter paper and the sample frozen in liquid-nitrogen-cooled ethane. The grids were transferred with a Gatan cryo-holder 626 in a Philips CM 12 microscope operated at 80 kV. Images were recorded at a magnification of ×35,000 on a Kodak SO-63 developed for 12 min in D-19 developer at room temperature.

For image analysis, the quality of micrographs was checked by optical diffraction. Suitable micrographs were scanned with a Nikon Coolscan 8000 with a pixel size of 12.7 μm, corresponding to 0.363 nm at the specimen level. Particles were selected with the x3d program (7). Individual images were corrected for phase-contrast effects using the ctfit program (30).

All reconstructions were calculated using Imagic (48), except VLP6/7, for which the RIco program (35) was used. VLP6, VLP2/6, VLP2/6/7, DLP, and TLP images could be visually selected so that all particles had a constant diameter. When such a crude selection was applied to the VLP6, VLP2/6, and VLP2/6/7 images and the data sets were further processed, a convergent solution was rapidly obtained (see Fig. 3a [upper reconstruction] and b [upper and lower reconstructions], respectively). VLP6/7 represent a special case. Although all objects display a rather constant diameter, most particles show large deviations from icosahedral symmetry. As an attempt to overcome this limitation, we slowed down the VLP6/7 reassembly process by performing the reaction at 4°C, which did not result in any major improvement of the particle icosahedral symmetry. Because the particles are all spherical and show similar diameters, we hypothesized that they obey icosahedral symmetry but show local disorder (e.g., some VP6 and/or VP7 subunits were missing in their respective layers). To select the particles that best obey icosahedral symmetry, we used RIco, a program that expands the density in spherical harmonics and allows the calculation of a low-resolution reconstruction with a single view (35). Comparison of the reconstruction projections with the raw image permits selection of the particles obeying icosahedral symmetry. Starting with a few hundred images, we selected the 15 best images to calculate the VLP6/7 reconstruction (see Fig. 3a, lower reconstruction).

Images analyzed with Imagic were first normalized for their gray-level distribution and band path filtered, including information between 1/100 and 1 nm^{-1}. Processing was then carried out as described in the Imagic-5 manual. For the determination of the Euler angles and for the reconstruction, an icosahedral symmetry was assumed. The resolution of the reconstructions was estimated by Fourier shell correlation of two independent maps, each calculated with half of the data, as the spatial frequency where the correlation coefficient drops to 0.5.

The 3-D reconstruction done with RIco (http://www.hotreference.com/estrozi/RIco) was achieved in three main steps: preparation of the data, search of the Euler angles corresponding to the views, and building of the final reconstruction. First, the images were Fourier-Bessel transformed and sampled on 500 equidistant reciprocal pixels in the 0.0- to 0.5-nm^{-1} range. Only angular frequencies (Bessel orders) of below 130 were retained. Second, for each image and all possible view angles in 3-degrees steps, low-resolution icosahedral reconstructions were calculated using the first 120 sampling points (0.12 nm^{-1}) and including angular frequencies only up to 30. Each of these reconstructions was then projected and correlated to the original image. The view parameters of the best-correlated reconstruction were taken as a reference, and the view parameters of the rest of the images were redetermined and refined taking the reference into account. The center of each projection was also refined. Two important features of the reconstruction method are the following: first, no model is necessary, and second, substantially fewer images are necessary to produce the reconstructions (35). Another cycle of view/center refinement was carried out at higher resolution using angular frequencies of up to 50 and 200 reciprocal pixels (0.2 nm^{-1}). The third step consisted of building the final reconstruction from the oriented and centered images. For this, the complete Fourier-Bessel expansion was used up to a resolution of 2 nm. This procedure gave a map that was corrected for contrast transfer function (CTF) effects. The zeros of the CTF were searched as described previously (7). Phase-flip corrections were calculated for each group of images. To minimize the introduction of noise in the reconstructions, data near the zeros of the CTF functions were eliminated.

The reconstructions were calculated (Table 1) with the data contained in 50, 17, 106, 140, 184, and 182 images for the VLP6, VLP6/7, VLP2/6, VLP2/6/7, DLP, and TLP, respectively. The resolutions of the reconstructions were estimated by Fourier shell correlation, equal to 4.5, 4.0, 2.5, 2.8, 2.5, and 2.6 nm.

TABLE 1. Reconstruction parameters

Particle	Avg size (nm) ± SD[a]	Triangulation no.[b]	Resolution (nm)	No. of images	Channel I diam (nm)[c]
DLP	70.0 ± 1.3	13	2.5	184	4.1
TLP	76.5 ± 1.7	13	2.6	182	2.5
VLP2/6	70.6 ± 1.6	13	2.5	106	3.2
VLP2/6/7	75.7 ± 1.4	13	2.8	140	2.6
VLP6	80.1 ± 3.9	≥19	4.5	50	2.0
VLP6/7	82.3 ± 2.4	19	4.0	17	1.3

[a] The average sizes were measured on the micrographs and not on the reconstructions to minimize the bias of the particle selection.
[b] The triangulation numbers refer to that of the VP6 layer.
[c] The diameter channel was measured in the reconstruction by fitting the largest sphere that can be positioned on the fivefold axis without overlapping the VP6 atoms.

Figures of maps were rendered using the program PyMOL (http://www.pymol.org).

Fitting of the atomic model into the virus-like and viral particle reconstructions. The VP6 atomic model was fitted in all our reconstructions, i.e., VLP6, VLP6/7, VLP2/6, VLP2/6/7, DLP, and TLP, using the UROX software (http://mem.ibs.fr/UROX). The fit was performed in reciprocal space, taking into account the symmetry of the reconstruction. This allows the whole EM map to be used without applying a mask around individual molecules in the EM map, as often is the case in real-space refinement procedures. The quality of the fit was evaluated by applying a radial mask defining the position of VP6 and calculating correlation coefficients and R factors. In all cases they are higher than 0.8 and lower than 0.4, respectively.

RESULTS AND DISCUSSION

All rotavirus genes that we expressed were cloned from the bovine RF strain. To exclude any particularity associated with that strain, we first determined the low-resolution structures of the viral particles and compared them to the simian ones studied previously (2, 39, 41, 50).

Visualization and 3-D reconstruction of TLP and DLP of the RF strain. Transcription-competent and -incompetent viral particles (DLP and TLP, respectively) of the rotavirus RF strain were visualized by cryo-EM, and their structures were determined at resolutions of about 2 nm (Fig. 1). The 3-D reconstructions of DLP and TLP (Fig. 1c and d, respectively) reveal the structural characteristics of their constituting protein layers. As for other rotavirus strains, each icosahedral protein layer is characterized by a different triangulation number: T = 1 for the innermost layer (VP2), T = 13*l* for the second layer (VP6), and T = 1 for the TLP outer layer (VP7 trimers covering VP6 trimers and VP4 dimeric spikes). Although the VP2 layer has a rather uniform density, the asymmetric unit appears to be made of two domains, suggesting that the layer is composed of 120 VP2 molecules. The TLP outer layer comprises 780 VP7 molecules and 60 VP4 dimers. The VP4 dimers are believed to arise from disordered VP4 trimers of which two monomers dimerize at a physiological pH (36) upon trypsin proteolysis (8, 11, 36, 51). The bovine RF rotavirus strain thus presents a structure similar to that of simian strains. However, the VP4 contrast appears smaller in the RF strain TLP reconstruction than in other strains, suggesting an enhanced fragility and a possible loss during virus purification. In agreement with this observation, VP4 of the RF rotavirus strain was barely visible either by cryo-EM (Fig. 1) or by conventional negative-staining EM or denaturing gel electrophoresis (data not shown), as opposed to the case for other strains (2).

Most importantly, although they are similar, the VP6 layers are not identical in TLP and DLP. The channels formed by VP6 trimers on the fivefold axes have smaller diameters in TLP than in DLP. The diameter shrinkage is best observed on central sections through the reconstructions (Fig. 1; see Fig. 4a, b, and c and the enlarged view of areas located near the fivefold axis shown in Fig. 5e [DLP] and f [TLP]), as has been previously observed (15, 24). The VP7-dependent channel opening can be directly correlated to the transcription competence of the particles and to the exit of nascent mRNA. To further analyze the effect of VP7 on the type I channel, we expressed the different proteins constituting the rotavirus capsid and analyzed their interactions.

Characterization of the assemblies formed by the rotavirus capsid proteins. Assemblies of rotavirus capsid proteins were isolated from an insect cell-baculovirus expression system. Sf9 insect cells were infected with up to three baculoviruses, each expressing a single rotavirus capsid protein. The following combinations were expressed: VP6; VP6 and VP7; VP2 and VP6; and VP2, VP6, and VP7. A few days after infection, rotavirus protein assemblies were extracted and purified. In all cases, cryo-EM revealed spherical particles (Fig. 2) that resemble either the mature viral particle (TLP) (Fig. 1b) or the virus depleted from the external layer (DLP) (Fig. 1a). For this reason, and independently of their different diameters as shown below, assemblies formed by the different rotavirus capsid proteins will be referred to as VLP followed by the structural protein numbers characterizing their composition, sepa-

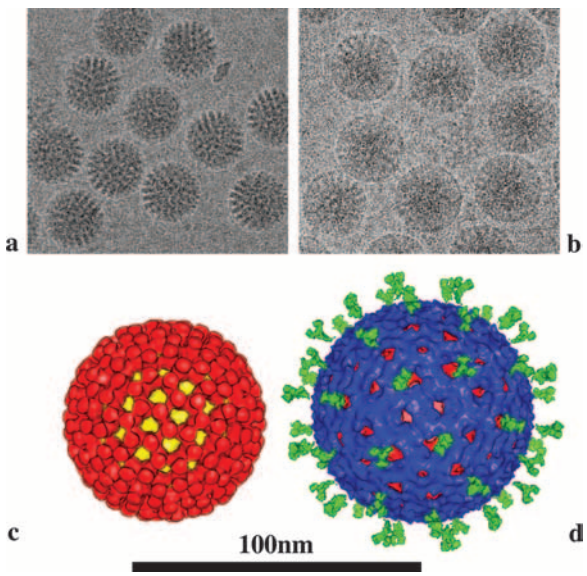

FIG. 1. Images and 3-D reconstructions of rotavirus particles. DLPs and TLPs were visualized by cryo-EM (a and b, respectively). The 3-D reconstructions at a resolution of about 2.5 nm show the layered structure of the particles (c and d). The DLP reconstruction shows two layers, made of VP2 (T = 1) and VP6 (T = 13) for the inner (yellow in panel c) and external (red in panel c) ones. The TLP reconstruction shows three layers made of VP2 (not visible on the figure, inside the red VP6 layer), VP6 (red in panel d), and VP7 (T = 13) (blue in panel d)-VP4 (T = 1) (green in panel d). The bars represent 100 nm (1,000 Å).

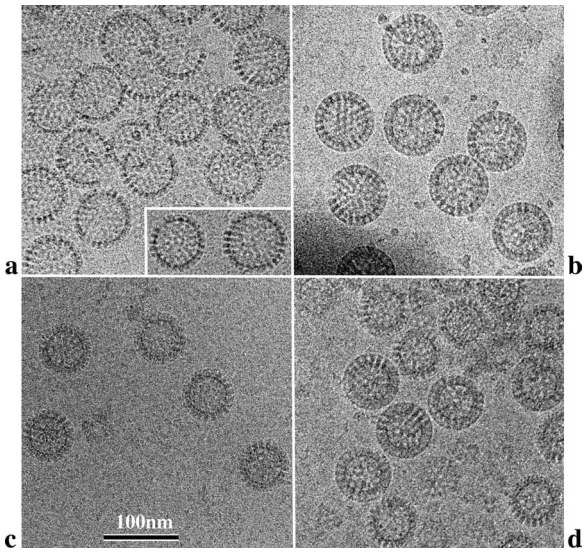

FIG. 2. Images of VLP6 (a), VLP6/7 (b), VLP2/6 (c), and VLP2/6/7 (d) visualized by cryo-EM. The inset shows two VLP6 particles having different diameters.

rated by slashes: VLP6 (Fig. 2a), VLP6/7 (Fig. 2b), VLP2/6 (Fig. 2c), and VLP2/6/7 (Fig. 2d).

Spherical VLP6 particles are formed in acidic conditions (pH 3.5 to 5.5) (27) but display various diameters and are always associated with partially assembled particles (Fig. 2a). Disassembly and reassembly of VLP6 by pH variation cycles did not change the heterogeneity of VLP6 samples, showing that, under these conditions, the VP6 trimer-trimer interactions are not specific to a particular assembly.

In the case of VP6 and VP7 coexpression, only a few assemblies appeared as VLP6/7 when they were directly observed after purification; most particles appeared as incomplete spheres (data not shown). In order to overcome this limitation, we found that VP6/VP7 particles are disassembled by chelating calcium with 1 mM EDTA and reassembled by addition of 10 mM $CaCl_2$. After one disassembly-assembly cycle, all particles appear as complete spherical VLP6/7 (Fig. 2b). It should be noted that while in the absence of calcium, helical assemblies of VP6 (27) are detected in VP6-VP7 samples (data not shown), in the presence of calcium, only VLP6/7 was observed by cryo-EM (Fig. 2b), independently of the pH value in the range 5 to 8. Together these observations show that VLP6 and VLP6/7 are labile particles built through rather weak protein-protein interactions. They also demonstrate that VP7 in the presence of calcium strongly drives the VP6 assembly process toward the formation of VLP, inhibiting the formation of VP6 helical assemblies.

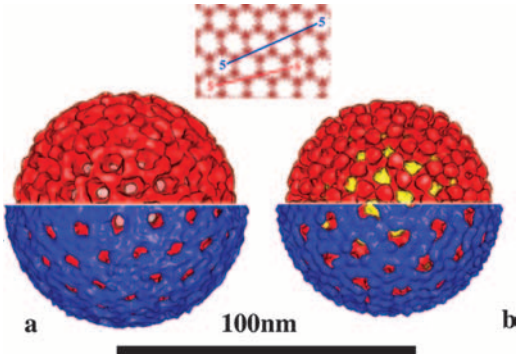

FIG. 3. 3-D reconstructions of VLPs. VLP6 (a, upper reconstruction) and VLP6/7 (a, lower reconstruction) show a T = 19 icosahedral lattice. The resolution of the VLP6 and VLP6/7 reconstructions is equal to about 4 nm (Table 1). VLP2/6 (b, upper reconstruction) and VLP2/6/7 (b, lower reconstruction) show T = 13 icosahedral symmetry. The resolution of the VLP2/6 and VLP2/6/7 reconstructions has a value close to 2.5 nm. Above the reconstructions is a schematic of the hexagonal lattice and the relative positioning of the fivefold axes. For T = 19 (blue), a walk from a fivefold axis to another one requires three and two steps along each lattice vector. For T = 13 (red), a walk from a fivefold axis to another one still requires three steps along one lattice vector but requires only one step along other one. The VP2, VP6, and VP7 layers are colored yellow, red, and blue, respectively.

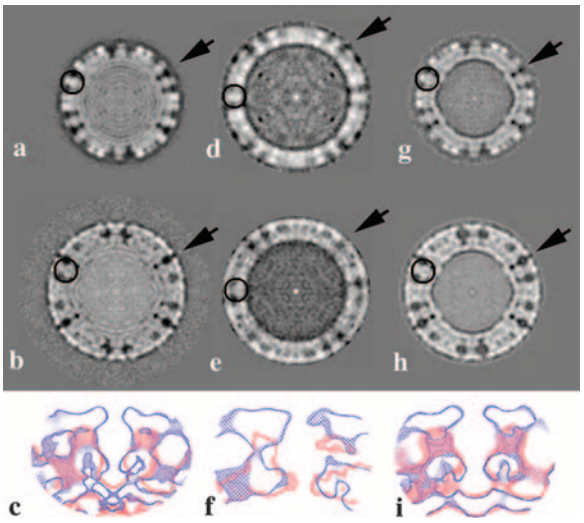

FIG. 4. Central section in the reconstructions of rotavirus particles DLP (a), TLP (b), VLP6 (d), VLP6/7 (e), VLP2/6 (g), and VLP2/6/7 (h). The section of a VP6 trimer is circled in all reconstruction. VP6 appears to be formed by two domains: the head and the base. A low-density area is present in the center of the base, in agreement with the X-ray model (31). The arrows indicate fivefold axes of the particle; the areas located near these axes shown in panels c, f, and i. When the reconstructions are scaled so that VP6 has same radial position in corresponding maps, the VP6 trimers around the fivefold axis appear to have different orientations and the type I channel to have different diameters, depending upon the presence of VP7. The fivefold axis areas are shown in panel c for DLP and TLP, in panel f for VLP6 and VLP6/7, and in panel i for VLP2/6 and VLP2/6/7. The reconstructions of particles containing VP7 are drawn in blue (c [TLP], f [VLP6/7], and i [VLP2/6/7]), while others are shown in red (c [DLP], f [VLP6], and i [VLP6/7]).

Each VLP has a distinctive appearance (number of rings and diameter) that is characteristic of its protein composition such that all protein layers of the rotavirus capsid can be visually recognized. Indeed, the VLPs containing VP2 or VP7 display a characteristic internal or external ring, respectively. VP6 forms a lattice displaying larger density variations than VP2 and VP7. Particles that contain VP7 (VLP6/7, VLP2/6/7, and TLP) thus have a smoother appearance (Fig. 1 and 2).

Remarkably, VP2 affects the curvature of the VLPs such that they have smaller diameters (Table 1). In contrast, VP7 increases the particle diameter by about 2.5 nm and signifi-

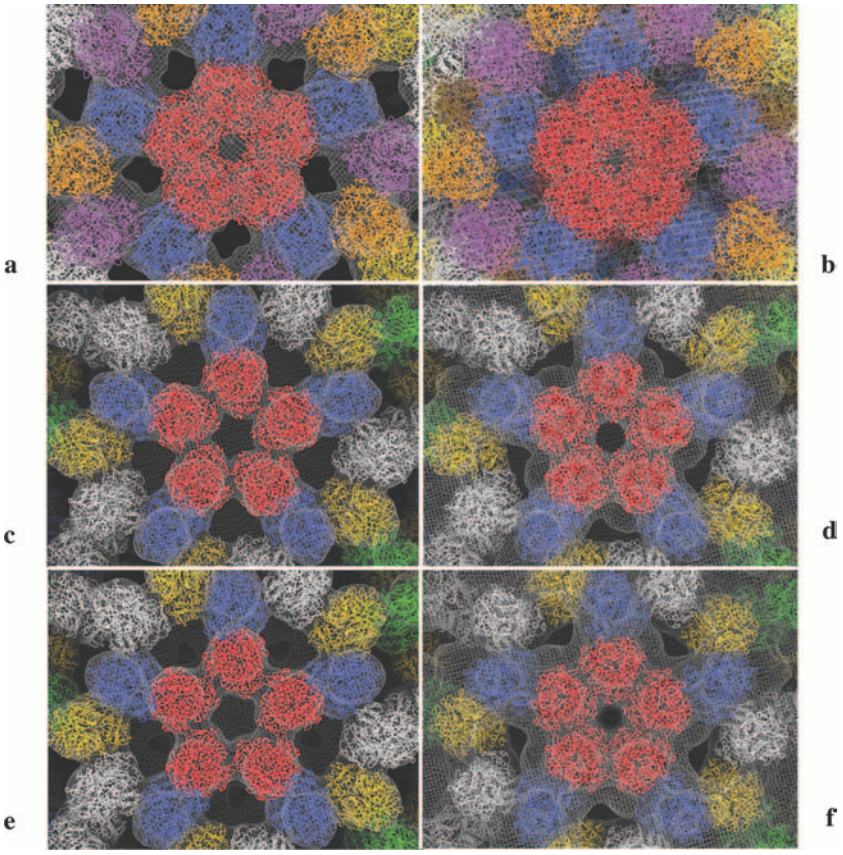

FIG. 5. Fitting of the X-ray model of VP6 into the cryo-EM maps for VLP6 (a), VLP6/7 (b), VLP2/6 (c), VLP2/6/7 (d), DLP (e), and TLP (f). Only the areas surrounding the type I channel are shown along the fivefold axis. The presence of VP7 results in a systematic reorientation of the VP6 trimers defining the type I channels. Here and in Fig. 6 and 7, the maps are shown in gray and the fitted models are arbitrarily colored, with the trimer closer to the fivefold axis in red.

cantly decreases the standard deviation of the diameter of VLPs formed in the absence of VP2 (Table 1). These data show that VP2 and VP7 constrain VP6 to form icosahedral layers having different geometries.

In order to better understand the VLP geometry and in particular the effect of VP2 and VP7 on the structure of the VP6 layer present in the different particles, we determined their 3-D structures.

3-D reconstruction of VLPs. Figure 3 shows the reconstructions of all studied VLPs. Although large structural variations could only be directly seen on VLP6 micrographs (Fig. 2), departures from icosahedral symmetry were found during the analysis of VLP6 as well as of VLP6/7. Only a few particles obeyed this symmetry; as a consequence, despite considerable efforts, the structures of both VLP6 and VLP6/7 could be determined only at a resolution of about 4 nm. Even though the resolutions are limited, the characteristic molecular envelope of the VP6 trimer could easily be recognized in the reconstructions (Fig. 3 and 4) and corresponds to that determined by X-ray crystallography (31). The VLP6 reconstructions (Fig. 3a, upper reconstruction) are characterized by a $T = 19$ triangulation number as seen from the VP6 distribution and associated fivefold and quasi-sixfold symmetry axis geometry. A central slice through the reconstruction (Fig. 4d) reveals that two domains form the VP6 molecule: the base, which is responsible for the contact between domains, and the head, which protrudes toward the exterior of the particle. Larger particles representing a minor fraction (less than 20%) were also observed in our preparations. Their low-resolution reconstructions obtained using a limited number of particles show that these larger particles obey a $T = 21$ triangulation number (data not shown). The presence of at least two different classes of VLP6 ($T = 19$ and $T = 21$) explains the rather large standard deviation observed previously for the diameter measurements.

The VLP6/7 reconstruction (Fig. 3a, lower reconstruction) also shows a characteristic $T = 19$ icosahedral symmetry, but only one class of particles was found in this case, as opposed to what was found during the VLP6 analysis. The central slice through the reconstruction (Fig. 4e) confirmed that the VLP6/7 particles are made of two protein layers. The inner layer is highly similar to the VLP6 reconstruction. The external one is constituted by trimeric entities that cover VP6 trimers. When the VLP6 and the VLP6/7 reconstructions are scaled so that the VP6 layers have the same radial positions in both maps, the main difference between the two reconstructions is the presence of the VP7 external layer (Fig. 4f).

The handedness of VLP6 and VLP6/7 lattices could not be determined using shadowing techniques (38) because both VLP6 and VLP6/7 are heavily damaged during drying even

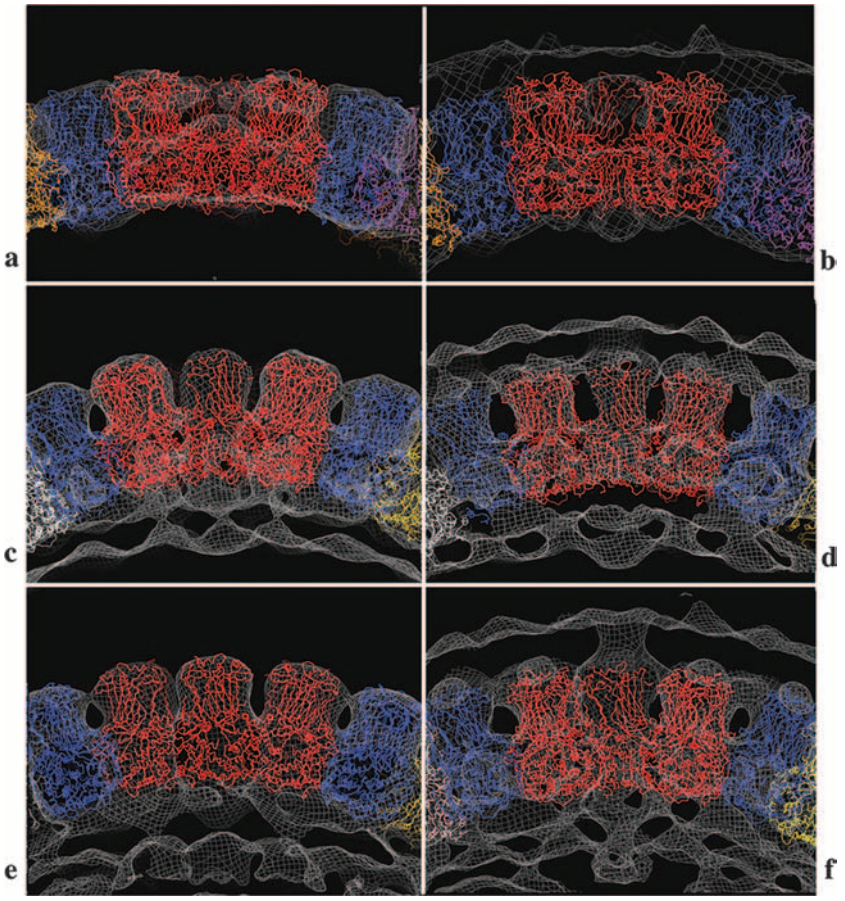

FIG. 6. Fitting of the VP6 atomic model into the cryo-EM maps for VLP6 (a), VLP6/7 (b), VLP2/6 (c), VLP2/6/7 (d), DLP (e), and TLP (f). A portion of the type I channel seen in a direction perpendicular to the fivefold axis. The layers above and below VP6 are VP7 and VP2, respectively.

when freeze-drying is used. However, fitting an X-ray crystallographic model of VP6 into these reconstructions (see below) indicates a slightly higher probability for a left-handed lattice that has thus been imposed on the VLP6 and VLP6/7 reconstructions.

The VLP2/6 and VLP2/6/7 reconstructions (Fig. 3b, upper and lower reconstruction, respectively) show that the presence of VP2 constrains the geometry of the VP6 and VP7 layers by imposing a T = 13 triangulation number. The handedness of the VLP2/6 and VLP2/6/7 was determined by the shadowing technique and was found to be identical to that of the virus (T = 13*l*; data not shown), as confirmed by fitting an X-ray model in the reconstructions, which indicates a higher probability for a left lattice. The VLP2/6 reconstruction is characterized by the presence of two protein layers that are best seen on a central slice (Fig. 4g). The VP2 layer is rather continuous and uniform and is covered by a T = 13 layer of VP6, showing trimeric VP6 molecules (Fig. 3b [upper reconstruction] and 4g) representing trimers of VP6. The VLP2/6 reconstructions were similar to those previously described (5, 26).

As expected, the VLP2/6/7 reconstruction shows three layers (Fig. 3b [lower reconstruction] and 4h): the inner and middle ones are similar to those that form VLP2/6, while the external layer displays trimers of VP7. When VLP2/6 and VLP2/6/7 are scaled so that VP2 and VP6 have identical radial positions in the two reconstructions, a small difference is visible on the channel located on the fivefold axes (Fig. 4i). In agreement with the TLP/DLP comparison, VLP2/6/7 presents type I channels having a smaller diameter than those of VLP2/6.

To better define the role of VP7 in the VP6 lattice, we fitted the atomic model of VP6 into our reconstructions.

Fit of the VP6 X-ray atomic model into VLP, DLP, and TLP reconstructions. The VP6 atomic model was fitted in each reconstruction using the UROX program. The fitting was performed in reciprocal space using the entire EM map without having to introduce a mask around individual molecules or protein layers. The fitting of VP6 in our DLP reconstruction is in agreement with previous results obtained using the simian DLP reconstruction (31). The VLP6 and VLP6/7 reconstructions contain 19 VP6 monomers (six trimers and a monomer) in the icosahedral asymmetric unit. In VLP2/6 and VLP2/6/7, the VP6 layer contains only 13 independent monomers (four trimers and a monomer). Despite the change in triangulation number between VLP6(/7) and VLP2/6(/7), the presence of VP7 leads in each case to a reorientation of the trimers around the fivefold axes and a shrinkage of the type I channel diameter (Fig. 5 and 6). Due to a better organization of the particles and

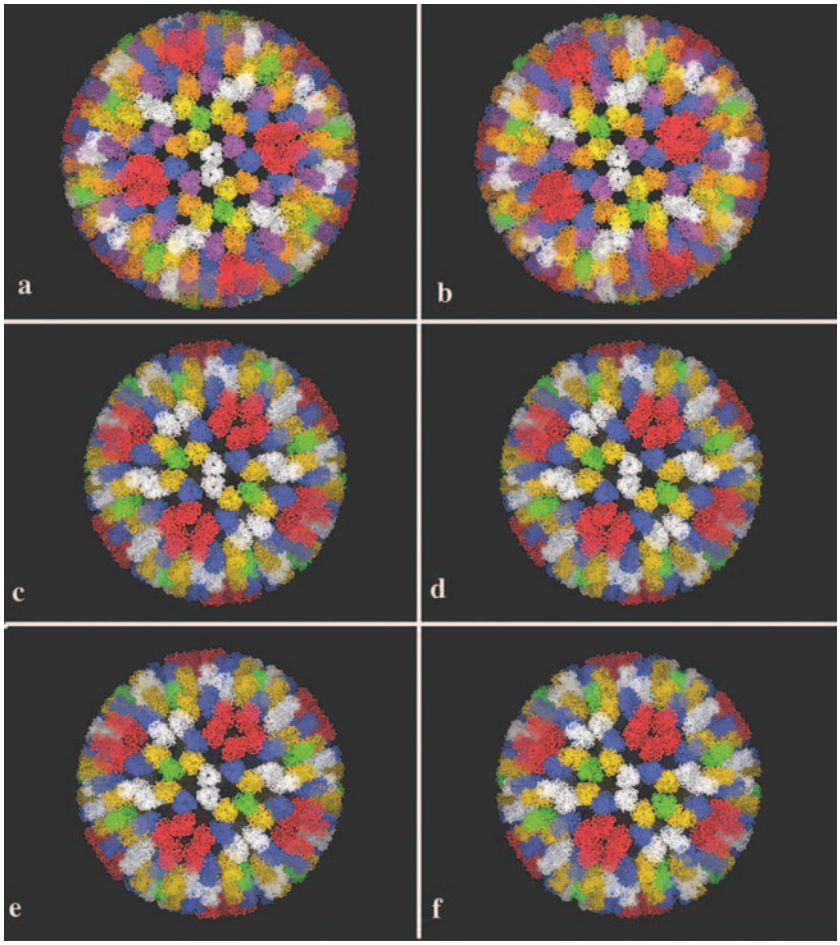

FIG. 7. Pseudo-atomic model of the VP6 layer for VLP6 (a), VLP6/7 (b), VLP2/6 (c), VLP2/6/7 (d), DLP (e), and TLP (f). VP6 trimers other than those located around fivefold axes display contacts that do not depend on the presence of VP7. The maps have been oriented so that the VP6 trimers near the twofold axis have similar orientations.

thus a better resolution of the reconstructions, the effect of VP7 on the VP6 lattice is better revealed when VP2 is present.

The comparison between the fits in the DLP and TLP (Fig. 5e and f and 6e and f) confirms the shrinkage of the fivefold axis channels observed in the VLP reconstructions. More precisely, VP7 induces a rotation of about 20 degrees and a radial displacement of more than 0.5 nm for the VP6 trimers flanking the fivefold axis, whereas the other VP6 trimers are only marginally affected by VP7. A VP7-induced rigid-body reorganization of the VP6 trimers suffices to explain the different diameters of the type I channels without the need to introduce substantial intratrimer rearrangement.

Figure 7 shows the quasi-atomic model of the VP6 layers of all the particles studied: VLP6 (Fig. 7a), VLP6/7 (Fig. 7b), VLP2/6 (Fig. 7c), VLP2/6/7 (Fig. 7d), DLP (Fig. 7e), and TLP (Fig. 7f). The diameter of the type I channel is systematically smaller when VP7 is present (Table 1).

The lattice polymorphism of VP6: a potential regulator of the transcription process. Like many capsid proteins (9, 21), VP6 shows a rich structural polymorphism. The different assemblies formed by VP6 have been shown to depend upon the pH conditions (27). At low pH (3 to 5.5), VP6 forms spherical particles, and at higher pH, it forms two types of helical assemblies. While at near-neutral pH (6 to 7) tubes having a diameter of 75 nm are formed, smaller tubes having a diameter of 45 nm polymerize at a more basic pH (7 to 8.5). The 3-D reconstruction of the helical particles combined with the fitting of the VP6 atomic model into the experimental map showed that the different assemblies arise from VP6 trimers displaying highly similar conformations but establishing different contacts. No large conformational change of the VP6 trimer needs to be introduced to fill the calculated envelope of the molecule. The data we obtained for VLP (VLP6, VLP6/7, VLP2/6, and VLP2/6/7) and viral particles (DLP and TLP) confirmed these observations. The atomic model of VP6 considered as a rigid body fits well in all reconstructions determined at a resolution of 2 to 3 nm. The VP6 trimer thus appears as a rigid molecule presenting a rich lattice polymorphism that arises from alternative contacts between VP6 trimers that are dictated by the protonation state of the molecule and by the contacts with other capsid molecules (VP7 with the head and VP2 with the base). The constraints introduced by the other layers on the VP6 lattice have different strengths. In the presence of either VP2 or VP7, the VP6 assembly process loses the dependence on pH to give rise only to spherical particles, which are formed over a large range of pH (4 to 8). The lattice polymorphism of

VP6 is well illustrated by the fact that VP2 and VP7 impose different intertrimer contacts and thus different VP6 lattices: VP7 imposes a T = 19 lattice, and VP2 imposes a T = 13 icosahedral geometry. When both proteins interact with VP6, the VP2 constraints are predominant and a T = 13 icosahedral particle is formed. Due to a better structural preservation (presence of RNA) or a more precise assembly process, the differences in the VP6 lattices between VLP2/6 and VLP2/6/7 are further increased between DLP and TLP. The structural change introduced by VP7 on the DLP VP6 layer has already been observed (15, 24) and was interpreted as arising from a conformational change of VP6. The similarity of the molecular envelopes obtained in all our EM reconstructions and X-ray crystallography exclude large movements within the domains of VP6. Due to the limited resolution, we cannot exclude small local structural changes. Because the termini of VP6 are oriented toward the interior of the trimer, the N-terminal extremity cannot participate to the intertrimeric contacts adopting different conformations, as it is the case for polyomavirus and plant viruses (20, 28). Nevertheless, the fitting of the atomic model in the 3-D reconstructions shows that small rearrangements of the contact between VP6 trimers are sufficient to explain the differences observed. Further work carried out at higher resolution will determine if the different contacts of VP6 are associated with slight local conformational changes.

DLPs, in contrast to TLPs, have the capacity to transcribe dsRNA to give rise to mRNA (6). The presence of VP7 on viral particles inhibits the transcription capacity of viral particles, and several explanations have been advanced to explain this phenomenon (15, 24, 46). Our results suggest the existence of a novel transcription inhibition mechanism: the transcription activity of the DLP is regulated by VP7 through small reorganization of the VP6 trimer located around the particle fivefold axes. Recently, the structure of a human rotavirus strain (WA) that transcribed poorly in vitro showed that the VP6 trimers around the fivefold axes are missing (18), stressing the importance of these trimers forming the type I channel. The function of a biological complex (i.e., the transcription activity of rotavirus particles) thus appears to be regulated by the remarkable capacity of a protein (VP6) to make different contacts and thus different macromolecular assemblies, depending upon its bound partners (protons, proteins, etc.).

Conclusions. The proteins constituting the triple-layered icosahedral capsid of the rotavirus have the remarkable ability to form different lattices depending upon the stoichiometry and pH conditions. Using a combination of cryo-EM and of fitting X-ray models into the 3-D reconstructions, we studied the interplay between the three capsid layers and showed that the triangulation numbers characterizing the icosahedral symmetry of the VLPs shift from 19 (without VP2) to 13 (with VP2). In the absence of VP2, the outer-layer protein VP7 drives the assembly process toward the formation of VLP, inhibiting the formation of helical assemblies. While VLP6 particles show large variations in diameter, all VLP6/7 particles have similar diameters corresponding to a T = 19 icosahedral symmetry. The capacity of VP6 to form icosahedral particles having triangulation numbers equal to 13, 19, and higher depending upon the stoichiometry of the constituting proteins imposes constraints on the intermediate VP6 layer of viral particles DLP and TLP. We propose that these structural constraints constitute a potential regulator for the transcription activity of rotavirus particles.

ACKNOWLEDGMENTS

We thank Félix Rey for reading the manuscript.

Grants from CNRS, INRA, and Agence Nationale de la Recherche (ANR) funded this study. X.S. was supported by a Marie Curie International Reintegation Grant (IRG-021715).

REFERENCES

1. **Adrian, M., J. Dubochet, J. Lepault, and A. W. McDowall.** 1984. Cryo-electron microscopy of viruses. Nature **308:**32–36.
2. **Anthony, I. D., S. Bullivant, S. Dayal, A. R. Bellamy, and J. A. Berriman.** 1991. Rotavirus spike structure and polypeptide composition. J. Virol. **65:** 4334–4340.
3. **Benureau, Y., J. C. Huet, A. Charpilienne, D. Poncet, and J. Cohen.** 2005. Trypsin is associated with the rotavirus capsid and is activated by solubilization of outer capsid proteins. J. Gen. Virol. **86:**3143–3151.
4. **Caspar, D. L. D., and A. Klug.** 1962. Physical principles in the construction of regular viruses. Cold Spring Harbor Symp. Quant. Biol. **27:**1–24.
5. **Charpilienne, A., M. Nejmeddine, M. Berois, N. Parez, E. Neumann, E. Hewat, G. Trugnan, and J. Cohen.** 2001. Individual rotavirus-like particles containing 120 molecules of fluorescent protein are visible in living cells. J. Biol. Chem. **276:**29361–29367.
6. **Cohen, J., J. Laporte, A. Charpilienne, and R. Scherrer.** 1979. Activation of rotavirus RNA polymerase by calcium chelation. Arch. Virol. **60:**177–186.
7. **Conway, J. F., and A. C. Steven.** 1999. Methods for reconstructing density maps of "single" particles from cryoelectron micrographs to subnanometer resolution. J. Struct. Biol. **128:**106–118.
8. **Crawford, S. E., S. K. Mukherjee, M. K. Estes, J. A. Lawton, A. L. Shaw, R. F. Ramig, and B. V. Prasad.** 2001. Trypsin cleavage stabilizes the rotavirus VP4 spike. J. Virol. **75:**6052–6061.
9. **Crowther, R. A., N. A. Kiselev, B. Bottcher, J. A. Berriman, G. P. Borisova, V. Ose, and P. Pumpens.** 1994. Three-dimensional structure of hepatitis B virus core particles determined by electron cryomicroscopy. Cell **77:**943–950.
10. **Denisova, E., W. Dowling, R. LaMonica, R. Shaw, S. Scarlata, F. Ruggeri, and E. R. Mackow.** 1999. Rotavirus capsid protein VP5* permeabilizes membranes. J. Virol. **73:**3147–3153.
11. **Dormitzer, P. R., E. B. Nason, B. V. Prasad, and S. C. Harrison.** 2004. Structural rearrangements in the membrane penetration protein of a non-enveloped virus. Nature **430:**1053–1058.
12. **Dormitzer, P. R., Z. Y. Sun, G. Wagner, and S. C. Harrison.** 2002. The rhesus rotavirus VP4 sialic acid binding domain has a galectin fold with a novel carbohydrate binding site. EMBO J. **21:**885–897.
13. **Estes, M. K.** 2001. Rotavirus and their replication, p. 1747–1785. *In* D. M. Knipe and P. M. Howley (ed.), Fields virology, vol. 2. Lippincott Williams and Wilkins, Philadelphia, PA.
14. **Estes, M. K., D. Y. Graham, and B. B. Mason.** 1981. Proteolytic enhancement of rotavirus infectivity: molecular mechanisms. J. Virol. **39:**879–888.
15. **Feng, N., J. A. Lawton, J. Gilbert, N. Kuklin, P. Vo, B. V. Prasad, and H. B. Greenberg.** 2002. Inhibition of rotavirus replication by a non-neutralizing, rotavirus VP6-specific IgA mAb. J. Clin. Investig. **109:**1203–1213.
16. **Fiore, L., H. B. Greenberg, and E. R. Mackow.** 1991. The VP8 fragment of VP4 is the rhesus rotavirus hemagglutinin. Virology **181:**553–563.
17. **Franco, M. A., I. Prieto, M. Labbe, D. Poncet, F. Borras-Cuesta, and J. Cohen.** 1993. An immunodominant cytotoxic T cell epitope on the VP7 rotavirus protein overlaps the H2 signal peptide. J. Gen. Virol. **74:**2579–2586.
18. **Greig, S. L., J. A. Berriman, J. A. O'Brien, J. A. Taylor, A. R. Bellamy, M. J. Yeager, and A. K. Mitra.** 2006. Structural determinants of rotavirus subgroup specificity mapped by cryo-electron microscopy. J. Mol. Biol. **356:**209–221.
19. **Grimes, J. M., J. N. Burroughs, P. Gouet, J. M. Diprose, R. Malby, S. Zientara, P. P. Mertens, and D. I. Stuart.** 1998. The atomic structure of the bluetongue virus core. Nature **395:**470–478.
20. **Harrison, S. C., A. J. Olson, C. E. Schutt, and F. K. Wonkler.** 1978. Tomato bushy stunt virus at 2.9 Å resolution. Nature **276:**368–373.
21. **Krol, M. A., N. H. Olson, J. Tate, J. E. Johnson, T. S. Baker, and P. Ahlquist.** 1999. RNA-controlled polymorphism in the in vivo assembly of 180-subunit and 120-subunit virions from a single capsid protein. Proc. Natl. Acad. Sci. USA **96:**13650–13655.
22. **Labbe, M., A. Charpilienne, S. E. Crawford, M. K. Estes, and J. Cohen.** 1991. Expression of rotavirus VP2 produces empty corelike particles. J. Virol. **65:**2946–2952.
23. **LaMonica, R., S. S. Kocer, J. Nazarova, W. Dowling, E. Geimonen, R. D. Shaw, and E. R. Mackow.** 2001. VP4 differentially regulates TRAF2 signaling, disengaging JNK activation while directing NF-kappa B to effect rotavirus-specific cellular responses. J. Biol. Chem. **276:**19889–19896.
24. **Lawton, J. A., M. K. Estes, and B. V. Prasad.** 1999. Comparative structural analysis of transcriptionally competent and incompetent rotavirus-antibody complexes. Proc. Natl. Acad. Sci. USA **96:**5428–5433.

25. **Lawton, J. A., M. K. Estes, and B. V. Prasad.** 1997. Three-dimensional visualization of mRNA release from actively transcribing rotavirus particles. Nat. Struct. Biol. **4:**118–121.
26. **Lawton, J. A., C. Q. Zeng, S. K. Mukherjee, J. Cohen, M. K. Estes, and B. V. Prasad.** 1997. Three-dimensional structural analysis of recombinant rotavirus-like particles with intact and amino-terminal-deleted VP2: implications for the architecture of the VP2 capsid layer. J. Virol. **71:**7353–7360.
27. **Lepault, J., I. Petitpas, I. Erk, J. Navaza, D. Bigot, M. Dona, P. Vachette, J. Cohen, and F. A. Rey.** 2001. Structural polymorphism of the major capsid protein of rotavirus. EMBO J. **20:**1498–1507.
28. **Liddington, R. C., Y. Yan, J. Moulai, R. Sahli, T. L. Benjamin, and S. C. Harrison.** 1991. Structure of simian virus 40 at 3.8-A resolution. Nature **354:**278–284.
29. **Ludert, J. E., F. Gil, F. Liprandi, and J. Esparza.** 1986. The structure of the rotavirus inner capsid studied by electron microscopy of chemically disrupted particles. J. Gen. Virol. **67:**1721–1725.
30. **Ludtke, S. J., P. R. Baldwin, and W. Chiu.** 1999. EMAN: semiautomated software for high-resolution single-particle reconstructions. J. Struct. Biol. **128:**82–97.
31. **Mathieu, M., I. Petitpas, J. Navaza, J. Lepault, E. Kohli, P. Pothier, B. V. Prasad, J. Cohen, and F. A. Rey.** 2001. Atomic structure of the major capsid protein of rotavirus: implications for the architecture of the virion. EMBO J. **20:**1485–1497.
32. **Mendez, I., L. Hermann, P. Hazelton, and K. Coombs.** 2000. A comparative analysis of freon substitutes in the purification of reovirus and calicivirus. J. Virol. Methods **90:**59–67.
33. **Nakagawa, A., N. Miyazaki, J. Taka, H. Naitow, A. Ogawa, Z. Fujimoto, H. Mizuno, T. Higashi, Y. Watanabe, T. Omura, R. H. Cheng, and T. Tsukihara.** 2003. The atomic structure of rice dwarf virus reveals the self-assembly mechanism of component proteins. Structure **11:**1227–1238.
34. **Nandi, P., A. Charpilienne, and J. Cohen.** 1992. Interaction of rotavirus particles with liposomes. J. Virol. **66:**3363–3367.
35. **Navaza, J.** 2003. On the three-dimensional reconstruction of icosahedral particles. J. Struct. Biol. **144:**13–23.
36. **Pesavento, J. B., S. E. Crawford, E. Roberts, M. K. Estes, and B. V. Prasad.** 2005. pH-induced conformational change of the rotavirus VP4 spike: implications for cell entry and antibody neutralization. J. Virol. **79:**8572–8580.
37. **Petitpas, I., J. Lepault, P. Vachette, A. Charpilienne, M. Mathieu, E. Kohli, P. Pothier, J. Cohen, and F. A. Rey.** 1998. Crystallization and preliminary X-ray analysis of rotavirus protein VP6. J. Virol. **72:**7615–7619.
38. **Pous, J., C. Chevalier, M. Ouldali, J. Navaza, B. Delmas, and J. Lepault.** 2005. Structure of birnavirus-like particles determined by combined electron cryomicroscopy and X-ray crystallography. J. Gen. Virol. **86:**2339–2346.
39. **Prasad, B. V., J. W. Burns, E. Marietta, M. K. Estes, and W. Chiu.** 1990. Localization of VP4 neutralization sites in rotavirus by three-dimensional cryo-electron microscopy. Nature **343:**476–479.
40. **Prasad, B. V., R. Rothnagel, C. Q. Zeng, J. Jakana, J. A. Lawton, W. Chiu, and M. K. Estes.** 1996. Visualization of ordered genomic RNA and localization of transcriptional complexes in rotavirus. Nature **382:**471–473.
41. **Prasad, B. V., G. J. Wang, J. P. Clerx, and W. Chiu.** 1988. Three-dimensional structure of rotavirus. J. Mol. Biol. **199:**269–275.
42. **Reinisch, K. M., M. L. Nibert, and S. C. Harrison.** 2000. Structure of the reovirus core at 3.6 A resolution. Nature **404:**960–967.
43. **Roseto, A., J. Escaig, E. Delain, J. Cohen, and R. Scherrer.** 1979. Structure of rotaviruses as studied by the freeze-drying technique. Virology **98:**471–475.
44. **Ruiz, M. C., S. R. Alonso-Torre, A. Charpilienne, M. Vasseur, F. Michelangeli, J. Cohen, and F. Alvarado.** 1994. Rotavirus interaction with isolated membrane vesicles. J. Virol. **68:**4009–4016.
45. **Ruiz, M. C., A. Charpilienne, F. Liprandi, R. Gajardo, F. Michelangeli, and J. Cohen.** 1996. The concentration of $Ca2^{+}$ that solubilizes outer capsid proteins from rotavirus particles is dependent on the strain. J. Virol. **70:**4877–4883.
46. **Thouvenin, E., G. Schoehn, F. Rey, I. Petitpas, M. Mathieu, M. C. Vaney, J. Cohen, E. Kohli, P. Pothier, and E. Hewat.** 2001. Antibody inhibition of the transcriptase activity of the rotavirus DLP: a structural view. J. Mol. Biol. **307:**161–172.
47. **Tosser, G., M. Labbe, M. Bremont, and J. Cohen.** 1992. Expression of the major capsid protein VP6 of group C rotavirus and synthesis of chimeric single-shelled particles by using recombinant baculoviruses. J. Virol. **66:**5825–5831.
48. **van Heel, M., G. Harauz, E. V. Orlova, R. Schmidt, and M. Schatz.** 1996. A new generation of the IMAGIC image processing system. J. Struct. Biol. **116:**17–24.
49. **Yeager, M., J. A. Berriman, T. S. Baker, and A. R. Bellamy.** 1994. Three-dimensional structure of the rotavirus haemagglutinin VP4 by cryo-electron microscopy and difference map analysis. EMBO J. **13:**1011–1018.
50. **Yeager, M., K. A. Dryden, N. H. Olson, H. B. Greenberg, and T. S. Baker.** 1990. Three-dimensional structure of rhesus rotavirus by cryoelectron microscopy and image reconstruction. J. Cell Biol. **110:**2133–2144.
51. **Yoder, J. D., and P. R. Dormitzer.** 2006. Alternative intermolecular contacts underlie the rotavirus VP5* two- to three-fold rearrangement. EMBO J. **25:**1559–1568.